

GENDR: LIGHTEN GENERATIVE DETAIL RESTORATION

Yan Wang, Shijie Zhao*, Kexin Zhang, Junlin Li, Li Zhang

MMLab, ByteDance

{wangyan.my, zhaoshijie.0526}@bytedance.com

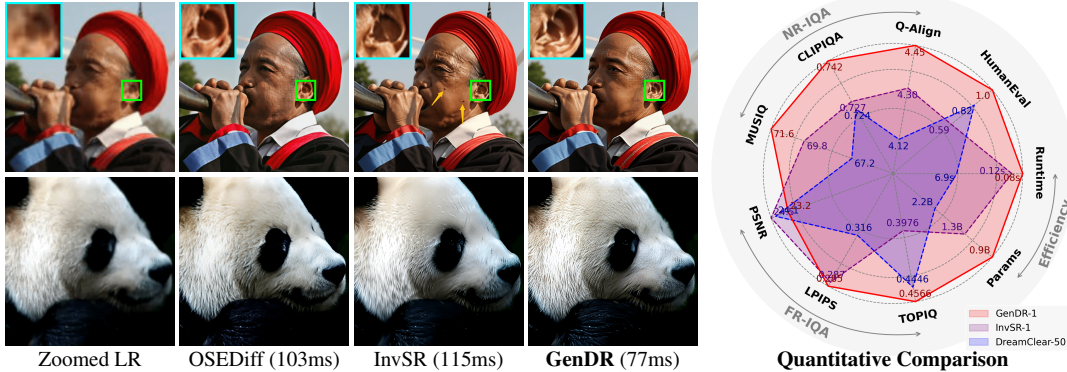


Figure 1: Visual comparison between proposed GenDR and recent state-of-the-art diffusion-based models (our method provides more details and higher fidelity with fewer time cost tested with 512^2 px on A100) (left) and quantitative comparison of representative SR methods (right), both of which demonstrate the advanced performance of the proposed GenDR. (Zoom in for best view.)

ABSTRACT

Although recent research applying text-to-image (T2I) diffusion models to real-world super-resolution (SR) has achieved remarkable progress, the misalignment of their targets leads to a suboptimal trade-off between inference speed and detail fidelity. Specifically, the T2I task requires multiple inference steps to synthesize images matching to prompts and reduces the latent dimension to lower generating difficulty. Contrariwise, SR can restore high-frequency details in fewer inference steps, but it necessitates a more reliable variational auto-encoder (VAE) to preserve input information. However, most diffusion-based SRs are multistep and use 4-channel VAEs, while existing models with 16-channel VAEs are overqualified diffusion transformers, *e.g.*, FLUX (12B). To align the target, we present a one-step diffusion model for generative detail restoration, GenDR, distilled from a tailored diffusion model with a larger latent space. In detail, we train a new SD2.1-VAE16 (0.9B) via representation alignment to expand the latent space without increasing the model size. Regarding step distillation, we propose consistent score identity distillation (CiD) that incorporates SR task-specific loss into score distillation to leverage more SR priors and align the training target. Furthermore, we extend CiD with adversarial learning and representation alignment (CiDA) to enhance perceptual quality and accelerate training. We also polish the pipeline to achieve a more efficient inference. Experimental results demonstrate that GenDR achieves state-of-the-art performance in both quantitative metrics and visual fidelity.

1 INTRODUCTION

Image super-resolution (SR) is a classical low-level problem to recover a high-resolution (HR) image from the low-resolution (LR) version (Dong et al., 2016; Lim et al., 2017). Its core aim is to repair missing high-frequency information from complex or unknown degradation in real-world scenarios with the help of learned priors. To reconstruct more realistically, the existing

*Corresponding Author.

methods SRGAN, RealESRGAN introduce generative adversarial networks (GAN) to reproduce the details and have revealed advanced performance. Recently, modernized text-to-image (T2I) models, *e.g.*, *Stable Diffusion* (SD) and *PixArt*, have demonstrated their ability to synthesize high-resolution images with photographic quality, offering a new paradigm to replenish details.

To assign an image SR objective to these T2I-oriented diffusion models, [Wang et al. \(2024b\)](#); [Lin et al. \(2024\)](#) leverage additional control modules such as controlnet and encoder to guide a T2I model to generate HR images from the noise. Although these methods exhibit superior restoration quality compared to GAN-based methods, two disturbing problems persist that restrict the practical usage of diffusion-based SR: *slow inference speed* and *inferior detail fidelity*. To address these issues, OSEDiff ([Wu et al., 2024b](#)) employs variational score distillation (VSD) ([Wang et al., 2024d](#)) through low-rank adaptation (LoRA) ([Hu et al., 2022](#)) to directly distill a one-step SR model from the T2I model, which significantly improves throughputs but weakens generation quality. Dream-Clear ([Ai et al., 2025](#)) employs two controlnets and MLLM-generated prompts to guide PixArt- α ([Chen et al., 2023a](#)), generating more faithful results. However, existing methods are caught in the dilemma that improving detail fidelity brings computational overhead (larger base model/additional assistant module), leading to inefficiency while accelerating inference results in unacceptable performance drop since they neglect critical underlying.

As shown in Fig. 2, we identify divergent task objectives between T2I *requiring more inference steps and low-dimensional latent space* and SR *requiring fewer inference steps and high-dimensional latent space* as the main contributors to the above problems. This finding is based on the following observations:

- *Divergent generating difficulty*: T2I models start from a sampled Gaussian noise to generate both low-frequency content and high-frequency details aligned with textual prompts. Nevertheless, the low-frequency structural and semantic components are well-defined in LR for the SR task, primarily demanding detail generation. Consequently, an ideal SR-tailored diffusion model can theoretically use fewer inference steps since it focuses on details and has no need to align with text.
- *Divergent reconstruction demands*: For T2I, expanding latent space inherently increases model complexity and training difficulty, leading most frameworks to adopt a 4-channel VAE to balance synthesis quality and computational efficiency. Although this trade-off optimizes performance for T2I, it becomes a barrier for reconstruction tasks like SR. VAE4s stumble to preserve intricate details within compressed latent representation, resulting in irreversible detail loss and structural distortion ([Dai et al., 2023](#); [Esser et al., 2024](#)).

To address these limitations holistically, this work provides a systematic solution, namely GenDR, for real-world super-resolution (SR), particularly targeting faithful and intricate Generative Detail Restoration. To build this model, we introduce several innovations:

- *Tailored Base Model*. Since SR tasks demand a larger latent space, we construct GenDR with a 16-channel base model. However, existing models (DiTs like SD3.5 and FLUX) are overqualified for generating details and prohibitively large to exacerbate the dilemma between quality and speed. For instance, to execute $\times 4$ SR for 256×256 input on a FLUX-based SR, the one-step processing costs over 40GB GPU memory and 1.4s runtime, which is $5.3 \times$ and $11.4 \times$ larger than SD2.1-based

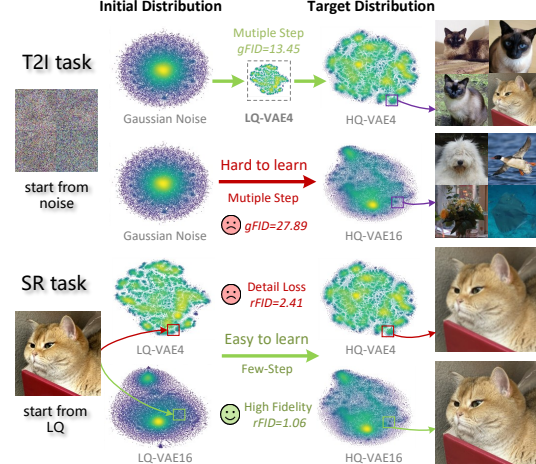


Figure 2: **Motivation**: divergent task objectives make dilemma. Compared to T2I task, SR task generates only details from LQ to HQ but needs to preserve more information from LQ, demanding fewer inference steps and larger latent capability. *We visualize the latent distribution on ImageNetval ImageNet with t-SNE*.

models. Thus, based on SD2.1 and an open-source VAE16, we construct an SD2.1-VAE16 as a suitable base model for diffusion-based restoration tasks.

- *Advanced Step Distillation.* To minimize the inference process to one step, we perform step distillation for GenDR. Unlike existing methods (Wu et al., 2024b; Sauer et al., 2024) that directly employ score distillation from T2I, we integrate task-specific consistent priors from SR into score identity distillation (SiD) (Zhou et al., 2024b), proposing Consistent score identity Distillation (CiD), which mitigates adverse effects caused by inconsistencies in the training distribution and over-reliance on imperfect score functions. Furthermore, we introduce CiDA, which incorporates CiD with representation Alignment and Adversarial learning to accelerate training and restore high-diversity details, avoiding the “fakeness” of AI-generated images. In practice, we apply low-rank adaptation (LoRA) and model-sharing strategies to implement the CiDA training scheme more efficiently.
- *Simplified Pipeline.* We construct a simplified diffusion pipeline comprised solely of VAE and UNet. We remove the scheduler and conditioning modules and use fixed textual embeddings to enable efficient deployment.

Overall, GenDR gains remarkable improvement over existing models in objective quality/efficiency metrics (Tab. 1), subjective visual comparison (Fig. 5), and human evaluation (Fig. 6).

2 RELATED WORK

2.1 GENERATIVE PRIOR FOR SR

Existing generative prior-based SR methods can be broadly categorized into GAN prior-based and diffusion prior-based paradigms. In detail, **GAN** can produce realistic synthesis by enforcing an adversarial updating between the discriminator and generator. Given the generator \mathcal{G} and discriminator \mathcal{D} , GAN cyclically optimizes them with varied adversarial losses:

$$\begin{aligned}\mathcal{L}^{\mathcal{D}} &= \mathbb{E}_{\mathbf{x}_h, \mathbf{x}_g = \mathcal{G}(\mathbf{x}_l)} [\ln(1 - \mathcal{D}(\mathbf{x}_g)) + \ln \mathcal{D}(\mathbf{x}_h)], \\ \mathcal{L}^{\mathcal{G}} &= \mathbb{E}_{\mathbf{x}_g} \ln \mathcal{D}(\mathbf{x}_g),\end{aligned}\tag{1}$$

where \mathbf{x}_g , \mathbf{x}_h , and \mathbf{x}_l are SR images, high-quality, and low-quality images for SR tasks. Based on the target, GAN-based SR models (Zhang et al., 2021; Wang et al., 2018) exploit adversarial training to synthesize visually pleasing details at the cost of occasional instability during optimization. As a milestone, Real-ESRGAN (Wang et al., 2021) introduced a high-order degradation datapipe to synthesize LR-HR training pairs.

Diffusion model decouples the image synthesis into forward and reverse processes in the latent space to stabilize the training and generated quality. For forward diffusion processing, the Gaussian noise $\epsilon \sim \mathcal{N}(0, \mathbf{I})$ is added with the time t -related variance $\beta_t \in (0, 1)$ to obtain the immediate latent $\mathbf{z} : \mathbf{z}_t = \bar{\alpha}_t \mathbf{z} + \bar{\beta}_t \epsilon$, where $\alpha_t = 1 - \beta_t$ and $\bar{\alpha}_t = \sqrt{\prod_{s=1}^t \alpha_s}$. During the reverse process, the diffusion model predicts the noise $\hat{\epsilon}$, thus obtaining the initial latent $\hat{\mathbf{z}}_0 = (\mathbf{z}_t - \bar{\beta}_t \hat{\epsilon}) / \bar{\alpha}_t$. For SR tasks, a better-starting node, *i.e.*, the LR image \mathbf{z}_l , can enable an efficient and simplified reverse function to calculate restored latent \mathbf{z}_g :

$$\mathbf{z}_g = \frac{\mathbf{z}_l - \bar{\beta}_{t_s} \epsilon_{\theta}(\mathbf{z}_l; t_s)}{\bar{\alpha}_{t_s}},\tag{2}$$

where ϵ_{θ} represents the noise-predicting network. Diffusion-based SR models (Wu et al., 2024c; Zhang et al., 2024; Ai et al., 2025; Yang et al., 2024) finetune base model (*e.g.*, UNet and DiT) or train an extra conditioning model (*e.g.*, Encoder and ControlNet) to guide iterative generation that aligns to the low-quality input. For instance, DiffBIR (Lin et al., 2024) introduced a preclear module and IRControlNet to balance fidelity and detail generation. FaithDiff (Chen et al., 2024b) fine-tuned an auxiliary encoder for SDXL (Rombach et al., 2022). Recently, Yi et al. (2025) proposed Transfer VAE Training (TVT), which tried to solve fidelity problem by training better VAE for diffusion pipeline, which achieves the same compression rate as GenDR.

2.2 STEP DISTILLATION

To reduce inference cost, massive research has focused on distilling multiple-step diffusion processes into few-step frameworks. As a pioneering work, DreamFusion (Poole et al., 2022) introduced score distillation sampling (SDS) to transfer knowledge from diffusion to arbitrary generators, which paves the way for step distillation. ProlificDreamer (Wang et al., 2024d) and Diff-instruct (Luo et al., 2023) utilized variational score distillation to enhance generation diversity and stability through probabilistic refinement. SiD (Zhou et al., 2024b) further ameliorated the score distillation with identity transformation for stable training.

3 METHODOLOGY

3.1 SD2.1-VAE16: 16-CHANNELS VAE MATTERS

To tailor a base model with a larger latent space for the SR task, we develop the UNet from SD2.1¹ in the latent space of 16-channel VAE². To speed up training, we conduct full-parameter optimization using the representation alignment strategy (Yu et al., 2024b). Given input image \mathbf{x}_h , intermediate latent \mathbf{z}_t , encoded output $\mathbf{h}_t = f_\theta(\mathbf{z}_t)$, REPA aligns projected results \mathbf{h}_t with the representation $\mathbf{h}_\mathcal{E} = \mathcal{E}(\mathbf{x}_h)$ obtained by pre-trained encoder \mathcal{E} , e.g. DINOv2 (Oquab et al., 2023):

$$\mathcal{L}^{(\text{rep})} = -\mathbb{E}_{\mathbf{x}_h, t} \left[\frac{1}{N} \sum_{n=1}^N \text{sim}(\mathbf{h}_\mathcal{E}[n], h(\mathbf{h}_t[n])) \right]. \quad (3)$$

In practice, we insert the multilayer perceptron (MLP) as h after the first downsampling block in UNet. To further improve the model’s comprehension of image quality attributes, *i.e.*, quality-assessment terminologies like *compressed* and *blurred*, we refine the base model following the DreamClear (Ai et al., 2025).

3.2 CiD: CONSISTENT SCORE IDENTITY DISTILLATION

The existing score distillation methods (Poole et al., 2022; Wang et al., 2024d; Zhou et al., 2024b) are based on the insight: *If generator \mathcal{G}_θ produces outputs \mathbb{P}_g approximating to real data distribution \mathbb{P}_r , the score model ψ trained by \mathbb{P}_g should converge to pretrained model ϕ trained by \mathbb{P}_r .*

Score distillation. Given the fixed real score model ϕ and updated fake score model ψ , the restoration network \mathcal{G}_θ , generated latent $\mathbf{z}_g = \mathcal{G}_\theta(\mathbf{z}_t)$, sampled timestep t , and noise ϵ , the VSD (Wang et al., 2024d) is to cyclicly update θ and ψ by:

$$\begin{aligned} \nabla_\theta \mathcal{L}_\theta^{(\text{vsd})} &= \mathbb{E}_{t, \epsilon, c, \mathbf{z}_t = \bar{\alpha}_t \mathbf{z}_g + \bar{\beta}_t \epsilon} \left[\omega(t)(\epsilon_\phi(\mathbf{z}_t; t, c) - \epsilon_\psi(\mathbf{z}_t; t, c)) \frac{\partial \mathbf{z}_g}{\partial \theta} \right], \\ \mathcal{L}_\psi &= \mathbb{E}_{t, \epsilon, c, \mathbf{z}_t} [||\epsilon_\psi(\mathbf{z}_t; t, c) - \epsilon||^2], \end{aligned} \quad (4)$$

where $\omega(t)$ is a time-aware weighting function. $\epsilon_{\phi, \psi}$ represents scores (noise) predicted by real/fake score networks. c indicates the prompt condition.

Score identity distillation. While VSD provides a tractable framework, it neglects the gradient of the fake score network and is difficult to ensure that ϵ_ψ achieves convergence, leading to unstable training and susceptibility to local optima due to inadequate convergence guarantees. Following Zhou et al. (2024b), we leverage score identity transformation to pre-estimate an ideal value $\epsilon_\psi(\mathbf{z}_t; t, c) = -\bar{\beta}_t \nabla_{\mathbf{z}_t} \log p_\theta(\mathbf{z}_t)$ for ϵ_ψ , incidentally reducing the dependence on ϵ_ψ :

$$\begin{aligned} \mathcal{L}_\theta^{(1)} &= \mathbb{E}_{t, \epsilon, c, \mathbf{z}_t = \bar{\alpha}_t \mathbf{z}_g + \bar{\beta}_t \epsilon} [||\epsilon_\phi(\mathbf{z}_t; t, c) - \epsilon_\psi(\mathbf{z}_t; t, c)||^2] \xrightarrow{\text{SiD}} \\ \mathcal{L}_\theta^{(2)} &= \mathbb{E}_{t, \epsilon, c, \mathbf{z}_t} [\omega(t) \langle \epsilon_\phi(\mathbf{z}_t; t, c) - \epsilon_\psi(\mathbf{z}_t; t, c), \epsilon_\phi(\mathbf{z}_t; t, c) - \epsilon \rangle]. \end{aligned} \quad (5)$$

Consistent score identity distillation. Despite effectiveness, the above-mentioned distillation strategies are tailored for the T2I task. The existing SR diffusion models, *e.g.*, ADDSR (Xie

¹huggingface: [stabilityai/stable-diffusion-2-1](#)

²huggingface: [ostris/vae-kl-f8-d16](#)

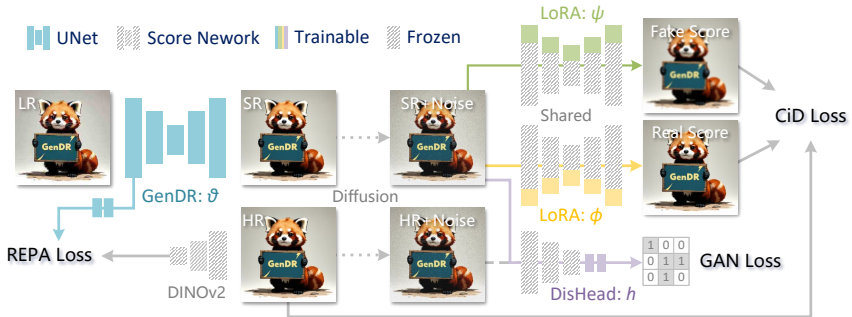


Figure 3: Illustration of the proposed CiDA training scheme for GenDR. GenDR and base score network are initialized with SD2.1-VAE16. The real and fake score networks are implemented by LoRA. LR latent is fed into GenDR to restore SR-latent and representation for REPA loss Eq. (3).

et al., 2024) and OSEDiff (Wu et al., 2024b) apply Eq. (4) directly as an additional loss of regularization without any specific modification. However, for the SR task, directly using Eqs. (4) and (5) poses difficulties since *T2I (aligning text embedding) and SR (aligning image embedding) have distinct targets and varying training distributions, leading to quality and content inconsistency*. Consequently, these methods employ regression loss (L1, MSE) to ensure consistency between generated latent \mathbf{z}_g and HR target \mathbf{z}_h :

$$\mathcal{L}_\theta^{(\text{mse})} = \mathbb{E}_{t,c} \left[\|\mathbf{z}_g - \mathbf{z}_h\|^2 \right]. \quad (6)$$

To address the issue, we optimize the “fixed” real score network ϕ with z_h to align its output distribution with the target high-fidelity image manifold, which ensures the real score network generates reliable priors for distillation. Following Zhou et al. (2024a), we regulate Eqs. (4) and (5) in latent space and introduce classifier-free guidance (CFG) (Ho & Salimans, 2022) with quality-related prompts to enhance guidance quality. Overall, the primary CiD can be formulated as follows:

$$\begin{aligned}
\mathcal{L}_\psi &= \mathbb{E}_{t, \epsilon, c, \mathbf{z}_t = \bar{\alpha}_t \mathbf{z}_g + \bar{\beta}_t \epsilon} [| | f_\psi(\mathbf{z}_t; t, c) - \mathbf{z}_g | |^2], \\
\mathcal{L}_\phi &= \mathbb{E}_{t, \epsilon, c, \mathbf{z}_t = \bar{\alpha}_t \mathbf{z}_h + \bar{\beta}_t \epsilon} [| | f_\phi(\mathbf{z}_t; t, c) - \mathbf{z}_h | |^2], \\
\tilde{\mathcal{L}}_\theta^{(2)} &= \mathbb{E}_{t, \epsilon, c, \mathbf{z}_t} [\omega(t) \langle f_{\phi, \kappa}(\mathbf{z}_t; t, c) - f_{\psi, \kappa}(\mathbf{z}_t; t, c), f_{\phi, \kappa}(\mathbf{z}_t; t, c) - \mathbf{z}_g \rangle], \tag{7}
\end{aligned}$$

where $f_{\phi, \psi}$ denotes scores (latent) predicted by real/fake score networks. $f_{\kappa}(\mathbf{z}_t; t, c) = f(\mathbf{z}_t; t, \emptyset) + \kappa \cdot [f(\mathbf{z}_t; t, c) - f(\mathbf{z}_t; t, \emptyset)]$, \emptyset represents empty prompt embeddings.

Similar to VSD and SiD, the above step distillation framework is data-free and relies on generated results \mathbf{z}_g , which introduce instability due to \mathbf{z}_g 's fluctuating quality and content. To mitigate this, we leverage the optimal latent for θ in Eq. (6) to replace \mathbf{z}_g with \mathbf{z}_h as an identity transformation.

$$\mathcal{L}_\theta^{(3)} = \mathbb{E}_{t, \epsilon, c, \mathbf{z}_t} [\omega(t) \langle f_{\phi, \kappa}(\mathbf{z}_t; t, c) - f_{\psi, \kappa}(\mathbf{z}_t; t, c), f_{\phi, \kappa}(\mathbf{z}_t; t, c) - \mathbf{z}_h \rangle]. \quad (8)$$

Overall, to circumvent the inability to compute $\nabla_{\theta}\psi$, we follow Zhou et al. (2024b); Huang et al. (2024) to combine $\mathcal{L}_{\theta}^{(1)}$ and $\mathcal{L}_{\theta}^{(3)}$ through empirical weighting ξ to ensure unbiased optimization:

$$\mathcal{L}_\theta^{(\text{cid})} = \mathcal{L}_\theta^{(3)} - \xi \mathcal{L}_\theta^{(1)}. \quad (9)$$

3.3 CiDA: CiD WITH ADVERSARY AND ALIGNMENT

Following DMD2 (Yin et al., 2024) and REPA (Yu et al., 2024b), we further develop the CiD (Eq. (9)) with adversarial learning and representation alignment. Based on Eq. (1), we examine the generated latent \mathbf{z}_g with pre-trained unet ϕ and extra discriminative heads h :

$$\mathcal{L}_\theta^{(\text{adv})} = \frac{1}{H'W'} \sum_{i=1}^{H'} \sum_{j=1}^{W'} \ln h(f_\phi(\mathbf{z}_g))[i, j], \quad (10)$$

where $H' \times W'$ denotes the spatial dimensions of the discriminator's output feature map.

We also reintroduce representation alignment in Eq. (3) as an effective regularization term. Combined with the CiD objective in Eq. (9) and adversarial loss in Eq. (10), the final target loss integrates:

$$\mathcal{L}_\theta^{(\text{cida})} = \lambda_1 \mathcal{L}_\theta^{(\text{cid})} + \lambda_2 \mathcal{L}_\theta^{(\text{adv})} + \lambda_3 \mathcal{L}_\theta^{(\text{repa})}, \quad (11)$$

where $\lambda_{1/2/3}$ are weighting coefficients balancing the contributions of distillation, adversarial, and alignment terms.

Implementation with LoRA. CiDA consists of one trainable generator and two trainable score networks, which cost huge GPU memory and computation resources for parameter updating across three UNets. To alleviate this burden, we utilize the low-rank adaptation (LoRA) [Hu et al. \(2022\)](#) for fake/real score networks to reduce the optimizable parameters. In addition, we share the base model for score networks and the feature extractor of the discriminator to further reduce the memory footprint of storing local models. In Fig. 3, we illustrate the detailed implementation of the proposed CiDA framework. In Sec. A.2, we present the detailed training schema for CiDA.

3.4 SIMPLIFIED DIFFUSION PIPELINE

To enable efficient inference without relying on complex preclear models or conditioning models, we design GenDR using a simplified architecture comprising only a UNet and VAE. Since GenDR executes a one-step calculation, we eliminate the scheduler by empirically assigning $\bar{\alpha}_t = \beta_t = 0.5$ across all timesteps t . Additionally, we discard the text encoder and tokenizer, replacing them with several fixed-prompt embeddings stored locally to reduce computational overhead and ensure deterministic generation. Fig. 4 shows the extremely laconic pipeline of GenDR.

4 EXPERIMENTS

4.1 EXPERIMENTAL SETUP

Training details. For SD2.1-VAE16, we train it on selected high-quality images ([Wang et al., 2022; Rombach et al., 2022](#)). The training resolution is 512×512 and 1024×1024 , which aligns to SD2.1-base and SDXL. We use ZeRO2-Offload ([Rajbhandari et al., 2020](#)) and gradient accumulation (steps=8) to extend the batch size to 2048 on 8 NVIDIA A100 GPUs. The fixed learning rate $1e^{-5}$, and default AdamW is adopted to optimize UNet during 100k iterations.

For GenDR, we initialize \mathcal{G}_θ and $f_{\phi,\psi}$ with SD2.1-VAE16-512px and conduct full parameter training for \mathcal{G}_θ on the LSDIR ([Li et al., 2023](#)), FFHQ ([Karras et al., 2019](#)), and above-selected images. As to $f_{\phi,\psi}$, we set LoRA rank and alpha as 64 and 128, respectively. Referring to previous setups ([Lin et al., 2024; Wu et al., 2024c;b](#)), we randomly crop 512×512 image patches to generate LR-HR pairs through a mixed pipeline of Real-ESRGAN ([Wang et al., 2021](#)) and APISR ([Wang et al., 2024a](#)). During 50k iteration training, networks are optimized via AdamW optimizers with batchsize 1024 and learning rate $1e^{-5}$ on 8 NVIDIA A100-80G. We set start-timestep $t_s = 500$ for GenDR, and randomly sample timesteps $t \in \{20, \dots, 979\}$ for CiDA score networks $f_{\phi,\psi}$. The loss coefficients $\lambda_{1,2,3}$ are 10 (first 10k)/1, 0.01, and 0.1, respectively. Specifically, we use $\omega(t) = C/\text{sg}[\|\mathbf{z}_h - f_{\phi,\psi}(\mathbf{z}_t; t, c)\|]$ as the time-related function to modulate CiDA loss.

Testing details. Following recent work ([Yue et al., 2024b](#)), we evaluate the proposed GenDR with the synthetic dataset ImageNet-Test ([Deng et al., 2009](#)) and several real-world test sets, RealSR ([Cai et al., 2019](#)), RealSet80 ([Yue et al., 2024b](#)), and RealLR200 ([Wu et al., 2024c](#)). The ImageNet-Test contains 3000 images under multiple complicated degradations. RealSR has 100 HR-LR image pairs taken by Nikon and Canon cameras. The RealSet80 and RealLR200 contain 80 and 200 low-resolution images without ground truth. In the test phase, we use official codes and settings to examine the

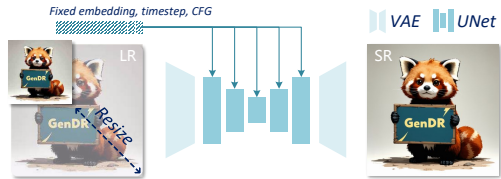


Figure 4: Illustration of proposed GenDR pipeline.

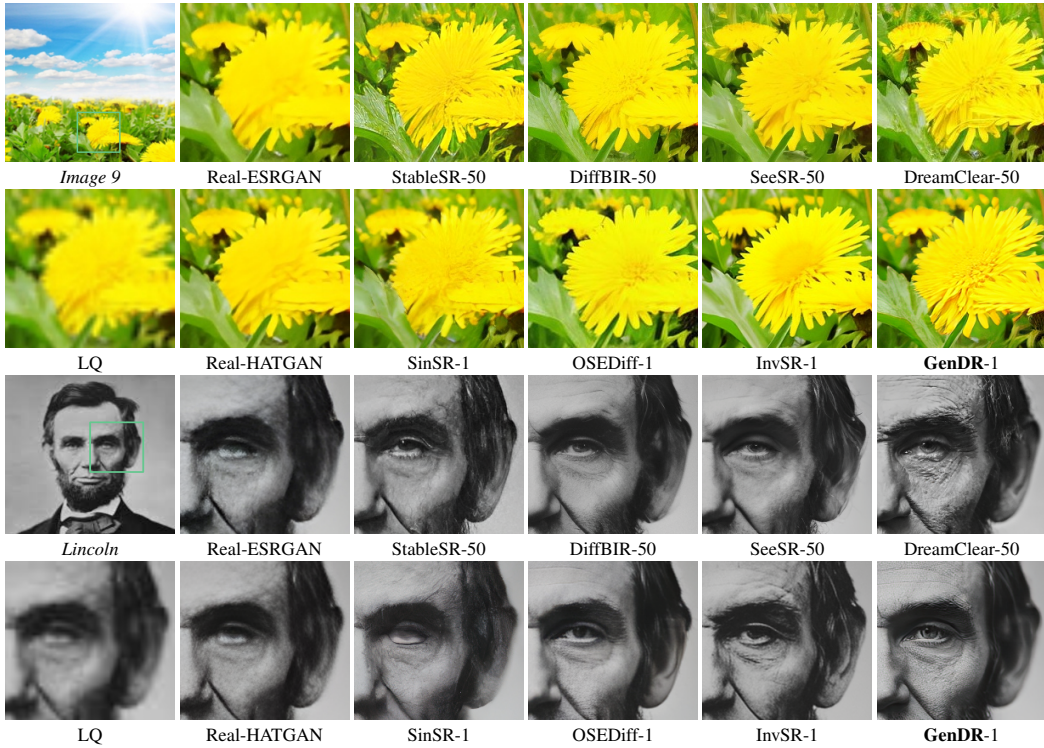


Figure 5: Visual comparison of GenDR with other methods for $\times 4$ task on RealSet80 dataset.

compared models for fairness. For GenDR, the positive/negative prompts are fixed to provide a general description³.

Evaluation metrics and compared methods. We leverage seven commonly used metrics to evaluate image quality, including full-reference metrics (FR-IQA): PSNR, SSIM (Wang et al., 2004), LPIPS (Zhang et al., 2018), and TOPIQ (Chen et al., 2024a), and no-reference metrics (NR-IQA): PI (Blau et al., 2018), NIQE (Mittal et al., 2012), LIQE (Zhang et al., 2023), MANIQA (Yang et al., 2022), ClipIQA (Wang et al., 2023), MUSIQ (Ke et al., 2021), ARNIQA (Agnolucci et al., 2024), Q-Align (Quality) (Wu et al., 2024a), and DeQA (You et al., 2025). We also conduct user and MLLM preference studies to obtain a comprehensive evaluation of image quality.

4.2 COMPARISON WITH STATE-OF-THE-ARTS

Quantitative comparison. To comprehensively evaluate the performance of GenDR, we compare it with numerous state-of-the-art methods, including GAN-based models: RealESRAN (Wang et al., 2021) and Real-HATGAN (Chen et al., 2023b), multiple-step diffusion models: StableSR (Wang et al., 2024b), DiffBIR Lin et al. (2024), SeeSR (Wu et al., 2024c), and DreamClear (Ai et al., 2025), one-step diffusion models: SinSR (Wang et al., 2024c), OSEDiff (Wu et al., 2024b), and InvSR (Yue et al., 2024a). Inclusively, our GenDR obtains superior restoration quality across all three benchmark datasets. As shown in Tab. 1, GenDR surpasses all existing one-step models by a large margin and can compete with multiple-step diffusion models. Specifically, GenDR achieves the highest LIQE, MUSIQ, and Q-Align on all benchmarks. Moreover, we add total parameters and inference time in Tab. 1, where the GenDR is the fastest and second smallest diffusion model. Compared to recent DreamClear, the GenDR gains about $89.5 \times$ acceleration and only uses half of the parameters.

Qualitative comparison. Fig. 5 exhibits the visual comparison for GenDR with other approaches. Generally, GenDR presents the best quality in terms of blurry removal and detail recovery. For *Image*

³“realism photo, best quality, realistic detailed, clean, high-resolution, best quality, smooth plain area, high-fidelity, clear edge, clean details without messy patterns, high-resolution, no noise, high-fidelity, 4K, 8K, perfect without deformations, photo taken in the style of Canon EOS-style raw”

Table 1: Quantitative comparison (average Parameters, Inference time, and IQA metrics) on both synthetic and real-world benchmarks. The sampling step number is marked in the format of “Method name-Steps” for diffusion-based methods. The best results for all methods are highlighted in **bold** and underlined, while the best one-step diffusion methods are reported in *italic*.

Methods	#Params↓	Metrics								
		PSNR↑	SSIM↑	LPIPS↓	NIQE↓	LIQE↑	ClipIQA↑	MUSIQ↑	Q-Align↑	
<i>ImageNet-Test</i>	Real-ESRGAN	GAN-CNN	26.62	0.7523	0.2303	4.4909	3.8414	0.5090	64.81	3.4230
	Real-HATGAN	GAN-Trans	27.15	0.7690	0.2044	4.7834	3.5717	0.4594	63.43	3.3244
	StableSR-50	SD 2.1-base	26.00	0.7317	0.2327	4.9378	3.6187	0.5768	64.54	3.4378
	DiffBIR-50	SD 2.1-base	25.45	0.6651	0.2876	4.9289	4.6378	0.7486	<u>73.04</u>	<u>4.3228</u>
	SeeSR-50	SD 2-base	25.73	0.7072	0.2467	4.3530	4.5384	0.6981	72.25	4.2412
	DreamClear-50	PixArt- α	24.76	0.6672	0.2463	5.3787	4.4298	0.7646	70.08	4.0919
	SinSR-1	LDM	26.98	0.7308	<u>0.2288</u>	5.2506	3.9410	0.6607	67.70	3.8090
	OSEDiff-1	SD 2.1-base	24.82	0.7017	0.2431	<u>4.2786</u>	<u>4.5609</u>	0.6778	71.74	4.0674
	InvSR-1	SD Turbo	23.81	0.6777	0.2547	4.3935	4.5601	0.7114	72.38	3.9867
	GenDR-1	SD 2.1-VAE16	24.14	0.6878	0.2652	4.1336	4.8096	0.7395	74.68	4.3612
<i>RealSR</i>	Real-ESRGAN	16.70M	25.85	0.7734	<u>0.2729</u>	4.6788	3.3372	0.4901	59.69	3.9185
	Real-HATGAN	20.77M	26.22	0.7894	0.2409	5.1189	2.8875	0.4336	58.41	3.8353
	StableSR-50	1410M	24.52	0.6733	0.3658	3.4665	3.5612	0.6897	66.87	3.9862
	DiffBIR-50	1717M	26.28	0.7251	0.3187	5.8009	3.3588	0.6743	64.28	3.9182
	SeeSR-50	2524M	26.19	0.7555	0.2809	4.5366	3.7728	0.6826	66.31	3.9862
	DreamClear-50	2212M	24.14	0.6963	0.3155	<u>3.9661</u>	3.5452	0.6730	63.74	3.9705
	SinSR-1	119M	25.99	0.7072	0.4022	6.2412	3.0034	0.6670	59.22	3.8800
	OSEDiff-1	1775M	24.57	0.7202	0.3036	4.3408	3.9634	0.6829	67.30	4.0664
	InvSR-1	1289M	24.50	0.7262	0.2872	4.2218	4.0346	<u>0.6919</u>	<u>67.47</u>	<u>4.2085</u>
	GenDR-1	933M	23.18	0.7135	0.2859	4.1588	4.1906	0.7014	68.36	4.2388
<i>RealSet80</i>	Methods	Runtime↓	Metrics							
			PI↓	ARNIQA↑	DeQA↑	NIQE↓	LIQE↑	ClipIQA↑	MUSIQ↑	Q-Align↑
	Real-ESRGAN	36ms	3.8843	0.6538	3.8906	4.1517	3.7392	0.6190	64.49	4.1696
	Real-HATGAN	116ms	4.1817	0.6578	3.8444	4.4705	3.4927	0.5502	63.21	4.1077
	StableSR-50	3731ms	3.0314	0.6776	3.8787	3.3999	3.8516	0.7399	67.58	4.0870
	DiffBIR-50	6213ms	3.9544	0.6802	4.0668	5.1389	4.0472	0.7404	68.72	<u>4.3206</u>
	SeeSR-50	6359ms	3.7454	0.7170	4.0728	4.3749	4.2797	0.7124	69.74	4.3056
	DreamClear-50	6892ms*	<u>3.4157</u>	0.6738	3.9429	<u>3.7257</u>	3.9628	0.7242	67.22	4.1206
	SinSR-1	120ms	4.2697	0.6638	3.9713	5.6103	3.5957	0.6634	63.79	4.0954
	OSEDiff-1	103ms	3.6894	0.6883	<u>4.0916</u>	3.9763	4.1298	0.7037	69.19	4.3057
	InvSR-1	115ms	<u>3.4524</u>	<u>0.7172</u>	4.0045	4.0266	4.2906	0.7271	<u>69.79</u>	4.3014
	GenDR-1	77ms	3.5518	0.7321	4.1289	3.9750	4.5248	0.7424	71.57	4.4525

*: inference time calculated under using 3 A100 GPU to run an image.

9 from RealSet80, GenDR is the only model to restore the entire chrysanthemum and correctly split foreground and background. As to *Image Lincoln*, GenDR recovers clearer eyes and more natural skin from the degraded input. The visual results demonstrate the splendid recovery performance of the proposed GenDR. In Sec. A.4.4, we provide more visual comparisons.

User studies and MLLM evaluation.

For a thorough comparison between diffusion-based SR, we conduct user studies to compare images restored by GenDR against SinSR, OSEDiff, and DreamClear. Fig. 6 shows that our GenDR convincingly outperforms other diffusion-based models. For further evaluation, we use MLLMs like Q-Align and DeQA, to enable human-like evaluation. Particularly, GenDR surpasses the second place by a large margin. Compared to recent InvSR, Q-Align and DeQA are improved by 0.12 and 0.15.

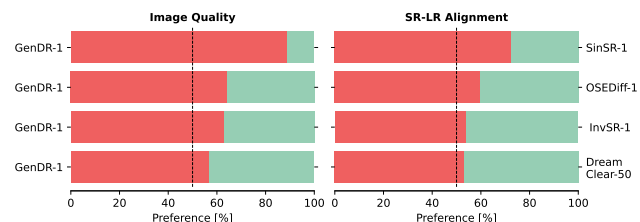


Figure 6: User studies on image quality and alignment.

Table 2: Ablation study on varied step distillation strategy for OSEDiff and GenDR on RealSet80.

SD2.1	Strategy	Metrics↑			
		LIQE	ClipIQA	MUSIQ	Q-Align
VAE4	VSD	4.1298	0.7037	69.19	4.3057
	CiDA	4.3184	0.7230	70.13	4.3858
	VSD	4.1248	0.6911	68.82	4.3732
	SiD	4.2528	0.7016	69.33	4.3912
	CiD	4.4432	0.7150	70.61	4.4278
	CiDA	4.5248	0.7424	71.57	4.4525

Table 3: Ablation study on varied prompt generating setting for GenDR.

Method	Prompt Extract	Prompt Embed	Time	#Params	#MACs	MUSIQ
Null	-	15ms	92ms	1263M	1637G	70.66
DAPE	21ms	15ms	113ms	1775M	2638G	71.74
Qwen2.5	3.09s	16ms	3.18s	8.3B	-	71.08
Fixed	-	15ms	92ms	1263M	1637G	71.57
Fixed	-	-	77ms	933M	1623G	71.57

Table 4: Quantitative comparison between stable diffusions on 20k prompts from COCO 2014.

Methods	GenEval↑							FID↓
	Overall	Single Obj.	Two Obj.	Counting	Colors	Position	Color Attr.	
SD1.5	0.43	0.97	0.38	0.38	0.76	0.04	0.06	13.45
SD2.1	0.50	0.98	0.51	0.44	0.85	0.07	0.17	13.45
SD2.1-VAE16	0.48 (-0.02)	0.98	0.53	0.35	0.79	0.08	0.12	27.89 (+14.44)
SDXL	0.55	0.98	0.74	0.39	0.85	0.15	0.23	18.4

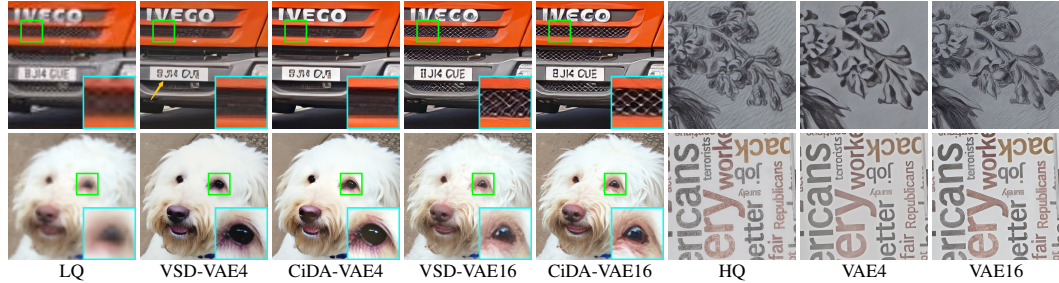


Figure 7: Visual comparison between VAE4 and VAE16, VSD and CiDA on RealSet80 and RealSR.

4.3 ABLATION STUDY

Effectiveness of CiD and CiDA. To examine the effectiveness of the proposed distillation approach, we use VSD (Wang et al., 2024d), SiD (Zhou et al., 2024b), CiD, and CiDA to distill SD2.1 (OSEDiff) and SD2.1-VAE16 (GenDR). Tab. 2 shows the quantitative comparisons, where the proposed CiDA yields a 0.08 improvement on Q-Align for both OSEDiff and GenDR. Specific to each loss function, the CiD accounts for 0.05 on Q-Align, and adversarial learning contributes the remaining 0.03. In Fig. 7, we provide a visual comparison for models trained by CiDA and VSD, where CiDA can provide vivid details and alleviate structural distortion.

Effectiveness of 16 channel VAE. Since GenDR is based on proposed SD2.1-VAE16, we first evaluate the new SD2.1-VAE16 in Tab. 4 by calculating GenEval (Ghosh et al., 2023) and FID on COCO 2014 (Lin et al., 2014), where the performance of SD2.1-VAE16 slightly decreases compared to SD2.1, indicating that in the T2I task, 4-channel VAE4 is more preferable than 16-channel for SD2.1. However, the performance reverses in the SR task. As exhibited in Tab. 2, compared to the 4-channel VAE model, SD2.1-VAE16 has similar or even higher objective scores. Moreover, the subjective comparison in Fig. 7 shows that VAE16 preserves more details and generates faithfully. Specifically, in the upper left case, the SD2.1-VAE16-based model restores the license plate and inlet grille. The results demonstrate that applying a 16-channel VAE matters for even small diffusion UNet in the SR task.

Effectiveness of simplified pipeline. For more efficient inference, we replace the text encoding modules and scheduler in GenDR with fixed embeddings. In Tab. 3, we compare the proposed GenDR pipeline with different prompt extractors (DAPE (Wu et al., 2024c), Qwen2.5VL-7B (Team, 2024)) and strategies, where our design is the most efficient and maintains a similar IQA score with content-related prompts. We provide more results on prompt selection in Sec. A.4.1.

5 LIMITATIONS

Despite our studies demonstrating that VAE-16 can alleviate detail fidelity degradation in the SR task, even for 0.9B UNet, further study on VAE with larger latent channels is not included due to the validated effectiveness of 16-channel VAE and the high training expenses for entire SD models. Another limitation lies in the training cost of CiDA. While we use LoRA and deepspeed to optimize the training process, CiDA needs large GPU memory, which restricts its extension in DiT models.

6 CONCLUSION

This work presents GenDR for real-world SR by tailoring the T2I model in an SR-favored manner, *i.e.*, using high-dimensional latent space to preserve and generate more details and one-step inference to improve efficiency. In detail, we develop an SD2.1-VAE16 providing a better trade-off between reconstruction quality and efficiency. Based on it, we introduce a consistent score identity distillation (CiD) that incorporates SR priors into T2I-oriented step diffusion to promote consistency and stability. Moreover, we improve CiD with adversarial learning and REPA to achieve better realistic details. Overall, GenDR obtains a remarkable quality-efficiency trade-off.

REFERENCES

Lorenzo Agnolucci, Leonardo Galteri, Marco Bertini, and Alberto Del Bimbo. Arniqa: Learning distortion manifold for image quality assessment. In *WACV*, pp. 189–198, 2024. [7](#)

Yuang Ai, Xiaoqiang Zhou, Huaibo Huang, Xiaotian Han, Zhengyu Chen, Quanzeng You, and Hongxia Yang. Dreamclear: High-capacity real-world image restoration with privacy-safe dataset curation. *NeurIPS*, 37:55443–55469, 2025. [2](#), [3](#), [4](#), [7](#)

Yochai Blau, Roey Mechrez, Radu Timofte, Tomer Michaeli, and Lihi Zelnik-Manor. The 2018 pirm challenge on perceptual image super-resolution. In *ECCVW*, pp. 0–0, 2018. [7](#)

Jianrui Cai, Hui Zeng, Hongwei Yong, Zisheng Cao, and Lei Zhang. Toward real-world single image super-resolution: A new benchmark and a new model. In *ICCV*, pp. 3086–3095, 2019. [6](#)

Chaofeng Chen, Jiadi Mo, Jingwen Hou, Haoning Wu, Liang Liao, Wenxiu Sun, Qiong Yan, and Weisi Lin. Topiq: A top-down approach from semantics to distortions for image quality assessment. *IEEE TIP*, 2024a. [7](#)

Junsong Chen, Jincheng Yu, Chongjian Ge, Lewei Yao, Enze Xie, Yue Wu, Zhongdao Wang, James Kwok, Ping Luo, Huchuan Lu, et al. Pixart- α : Fast training of diffusion transformer for photorealistic text-to-image synthesis. *arXiv preprint arXiv:2310.00426*, 2023a. [2](#)

Junyang Chen, Jinshan Pan, and Jiangxin Dong. Faithdiff: Unleashing diffusion priors for faithful image super-resolution. *arXiv preprint arXiv:2411.18824*, 2024b. [3](#)

Xiangyu Chen, Xintao Wang, Jiantao Zhou, Yu Qiao, and Chao Dong. Activating more pixels in image super-resolution transformer. In *CVPR*, pp. 22367–22377, June 2023b. [7](#)

Xiaoliang Dai, Ji Hou, Chih-Yao Ma, Sam Tsai, Jiali Wang, Rui Wang, Peizhao Zhang, Simon Vandenhende, Xiaofang Wang, Abhimanyu Dubey, et al. Emu: Enhancing image generation models using photogenic needles in a haystack. *arXiv preprint arXiv:2309.15807*, 2023. [2](#)

Jia Deng, Wei Dong, Richard Socher, Li-Jia Li, Kai Li, and Li Fei-Fei. Imagenet: A large-scale hierarchical image database. In *CVPR*, pp. 248–255, Miami, USA, 2009. IEEE Computer Society. [6](#)

Chao Dong, Chen Change Loy, Kaiming He, and Xiaoou Tang. Image super-resolution using deep convolutional networks. *IEEE TPAMI*, 38(2):295–307, 2016. [1](#)

Patrick Esser, Sumith Kulal, Andreas Blattmann, Rahim Entezari, Jonas Müller, Harry Saini, Yam Levi, Dominik Lorenz, Axel Sauer, Frederic Boesel, et al. Scaling rectified flow transformers for high-resolution image synthesis. In *ICML*, 2024. [2](#), [20](#)

Dhruba Ghosh, Hannaneh Hajishirzi, and Ludwig Schmidt. Geneval: An object-focused framework for evaluating text-to-image alignment. *NeurIPS*, 36:52132–52152, 2023. 9, 20

Jonathan Ho and Tim Salimans. Classifier-free diffusion guidance. *arXiv preprint arXiv:2207.12598*, 2022. 5

Edward J Hu, Yelong Shen, Phillip Wallis, Zeyuan Allen-Zhu, Yuanzhi Li, Shean Wang, Lu Wang, Weizhu Chen, et al. Lora: Low-rank adaptation of large language models. *ICLR*, 1(2):3, 2022. 2, 6

Zemin Huang, Zhengyang Geng, Weijian Luo, and Guo-jun Qi. Flow generator matching. *arXiv preprint arXiv:2410.19310*, 2024. 5

Tero Karras, Samuli Laine, and Timo Aila. A style-based generator architecture for generative adversarial networks. In *CVPR*, pp. 4401–4410, 2019. 6

Junjie Ke, Qifei Wang, Yilin Wang, Peyman Milanfar, and Feng Yang. Musiq: Multi-scale image quality transformer. In *CVPR*, pp. 5148–5157, 2021. 7

Xin Li, Kun Yuan, Bingchen Li, Fengbin Guan, Yizhen Shao, Zihao Yu, Xijun Wang, Yiting Lu, Wei Luo, Suhang Yao, et al. Ntire 2025 challenge on short-form ugc video quality assessment and enhancement: Methods and results. In *Proceedings of the Computer Vision and Pattern Recognition Conference*, pp. 1092–1103, 2025. 19

Yawei Li, Kai Zhang, Jingyun Liang, Jiezhang Cao, Ce Liu, Rui Gong, Yulun Zhang, Hao Tang, Yun Liu, Denis Demandolx, et al. Lsdir: A large scale dataset for image restoration. In *CVPRW*, pp. 1775–1787, 2023. 6

Bee Lim, Sanghyun Son, Heewon Kim, Seungjun Nah, and Kyoung Mu Lee. Enhanced deep residual networks for single image super-resolution. In *CVPRW*, pp. 1132–1140, 2017. 1

Tsung-Yi Lin, Michael Maire, Serge Belongie, James Hays, Pietro Perona, Deva Ramanan, Piotr Dollár, and C Lawrence Zitnick. Microsoft coco: Common objects in context. In *ECCV*, pp. 740–755. Springer, 2014. 9

Xinqi Lin, Jingwen He, Ziyan Chen, Zhaoyang Lyu, Bo Dai, Fanghua Yu, Yu Qiao, Wanli Ouyang, and Chao Dong. Diffbir: Toward blind image restoration with generative diffusion prior. In *ECCV*, pp. 430–448. Springer, 2024. 2, 3, 6, 7

Xinqi Lin, Fanghua Yu, Jinfan Hu, Zhiyuan You, Wu Shi, Jimmy S Ren, Jinjin Gu, and Chao Dong. Harnessing diffusion-yielded score priors for image restoration. *arXiv preprint arXiv:2507.20590*, 2025. 20

Weijian Luo, Tianyang Hu, Shifeng Zhang, Jiacheng Sun, Zhenguo Li, and Zhihua Zhang. Diff-instruct: A universal approach for transferring knowledge from pre-trained diffusion models. *NeurIPS*, 36:76525–76546, 2023. 4

Anish Mittal, Rajiv Soundararajan, and Alan C Bovik. Making a “completely blind” image quality analyzer. *IEEE Sign. Process. Letters*, 20(3):209–212, 2012. 7

Maxime Oquab, Timothée Darcet, Théo Moutakanni, Huy Vo, Marc Szafraniec, Vasil Khalidov, Pierre Fernandez, Daniel Haziza, Francisco Massa, Alaaeldin El-Nouby, et al. Dinov2: Learning robust visual features without supervision. *arXiv preprint arXiv:2304.07193*, 2023. 4

Bohao Peng, Jian Wang, Yuechen Zhang, Wenbo Li, Ming-Chang Yang, and Jiaya Jia. Controlnext: Powerful and efficient control for image and video generation. *arXiv preprint arXiv:2408.06070*, 2024. 20

Ben Poole, Ajay Jain, Jonathan T Barron, and Ben Mildenhall. Dreamfusion: Text-to-3d using 2d diffusion. *arXiv preprint arXiv:2209.14988*, 2022. 4

Samyam Rajbhandari, Jeff Rasley, Olatunji Ruwase, and Yuxiong He. Zero: Memory optimizations toward training trillion parameter models. In *SC20: International Conference for High Performance Computing, Networking, Storage and Analysis*, pp. 1–16. IEEE, 2020. 6

Robin Rombach, Andreas Blattmann, Dominik Lorenz, Patrick Esser, and Björn Ommer. High-resolution image synthesis with latent diffusion models. In *CVPR*, pp. 10684–10695, 2022. 3, 6, 20

Axel Sauer, Frederic Boesel, Tim Dockhorn, Andreas Blattmann, Patrick Esser, and Robin Rombach. Fast high-resolution image synthesis with latent adversarial diffusion distillation. In *SIGGRAPH Asia*, pp. 1–11, 2024a. 14

Axel Sauer, Dominik Lorenz, Andreas Blattmann, and Robin Rombach. Adversarial diffusion distillation. In *ECCV*, pp. 87–103. Springer, 2024b. 3

Qwen Team. Qwen2.5: A party of foundation models, September 2024. URL <https://qwenlm.github.io/blog/qwen2.5/>. 9, 16

Boyang Wang, Fengyu Yang, Xihang Yu, Chao Zhang, and Hanbin Zhao. Apisr: anime production inspired real-world anime super-resolution. In *CVPR*, pp. 25574–25584, 2024a. 6

Jianyi Wang, Kelvin CK Chan, and Chen Change Loy. Exploring clip for assessing the look and feel of images. In *AAAI*, volume 37, pp. 2555–2563, 2023. 7

Jianyi Wang, Zongsheng Yue, Shangchen Zhou, Kelvin CK Chan, and Chen Change Loy. Exploiting diffusion prior for real-world image super-resolution. *IJCV*, 132(12):5929–5949, 2024b. 2, 7

Xintao Wang, Ke Yu, Shixiang Wu, Jinjin Gu, Yihao Liu, Chao Dong, Yu Qiao, and Chen Change Loy. Esrgan: Enhanced super-resolution generative adversarial networks. In *ECCVW*, pp. 0–0, 2018. 3

Xintao Wang, Liangbin Xie, Chao Dong, and Ying Shan. Real-esrgan: Training real-world blind super-resolution with pure synthetic data. In *CVPR*, pp. 1905–1914, 2021. 3, 6, 7

Yufei Wang, Wenhan Yang, Xinyuan Chen, Yaohui Wang, Lanqing Guo, Lap-Pui Chau, Ziwei Liu, Yu Qiao, Alex C Kot, and Bihan Wen. Sinsr: diffusion-based image super-resolution in a single step. In *CVPR*, pp. 25796–25805, 2024c. 7

Zhengyi Wang, Cheng Lu, Yikai Wang, Fan Bao, Chongxuan Li, Hang Su, and Jun Zhu. Pro-lificdreamer: High-fidelity and diverse text-to-3d generation with variational score distillation. *NeurIPS*, 36, 2024d. 2, 4, 9, 18

Zhou Wang, Alan C. Bovik, Hamid R. Sheikh, and Eero P. Simoncelli. Image quality assessment: from error visibility to structural similarity. *IEEE TIP*, 13(4):600–612, 2004. 7

Zijie J Wang, Evan Montoya, David Munechika, Haoyang Yang, Benjamin Hoover, and Duen Horng Chau. Diffusiondb: A large-scale prompt gallery dataset for text-to-image generative models. *arXiv preprint arXiv:2210.14896*, 2022. 6

Haoning Wu, Zicheng Zhang, Weixia Zhang, Chaofeng Chen, Liang Liao, Chunyi Li, Yixuan Gao, Annan Wang, Erli Zhang, Wenxiu Sun, et al. Q-align: teaching lmms for visual scoring via discrete text-defined levels. In *ICML*, pp. 54015–54029, 2024a. 7

Rongyuan Wu, Lingchen Sun, Zhiyuan Ma, and Lei Zhang. One-step effective diffusion network for real-world image super-resolution. *NeurIPS*, 2024b. 2, 3, 5, 6, 7, 14, 18

Rongyuan Wu, Tao Yang, Lingchen Sun, Zhengqiang Zhang, Shuai Li, and Lei Zhang. Seesr: Towards semantics-aware real-world image super-resolution. In *CVPR*, pp. 25456–25467, 2024c. 3, 6, 7, 9, 16, 17

Rui Xie, Chen Zhao, Kai Zhang, Zhenyu Zhang, Jun Zhou, Jian Yang, and Ying Tai. Addsr: Accelerating diffusion-based blind super-resolution with adversarial diffusion distillation. *arXiv preprint arXiv:2404.01717*, 2024. 4

Sidi Yang, Tianhe Wu, Shuwei Shi, Shanshan Lao, Yuan Gong, Mingdeng Cao, Jiahao Wang, and Yujiu Yang. Maniq: Multi-dimension attention network for no-reference image quality assessment. In *CVPR*, pp. 1191–1200, 2022. 7

Tao Yang, Rongyuan Wu, Peiran Ren, Xuansong Xie, and Lei Zhang. Pixel-aware stable diffusion for realistic image super-resolution and personalized stylization. In *ECCV*, pp. 74–91. Springer, 2024. 3

Qiaosi Yi, Shuai Li, Rongyuan Wu, Lingchen Sun, Yuhui Wu, and Lei Zhang. Fine-structure preserved real-world image super-resolution via transfer vae training. In *ICCV*, pp. 12415–12426, 2025. 3

Tianwei Yin, Michaël Gharbi, Taesung Park, Richard Zhang, Eli Shechtman, Fredo Durand, and William T Freeman. Improved distribution matching distillation for fast image synthesis. *arXiv preprint arXiv:2405.14867*, 2024. 5, 14

Zhiyuan You, Xin Cai, Jinjin Gu, Tianfan Xue, and Chao Dong. Teaching large language models to regress accurate image quality scores using score distribution. *arXiv preprint arXiv:2501.11561*, 2025. 7

Fanghua Yu, Jinjin Gu, Zheyuan Li, Jinfan Hu, Xiangtao Kong, Xintao Wang, Jingwen He, Yu Qiao, and Chao Dong. Scaling up to excellence: Practicing model scaling for photo-realistic image restoration in the wild. In *CVPR*, pp. 25669–25680, 2024a. 17

Sihyun Yu, Sangkyung Kwak, Huiwon Jang, Jongheon Jeong, Jonathan Huang, Jinwoo Shin, and Saining Xie. Representation alignment for generation: Training diffusion transformers is easier than you think. *arXiv preprint arXiv:2410.06940*, 2024b. 4, 5

Zongsheng Yue, Kang Liao, and Chen Change Loy. Arbitrary-steps image super-resolution via diffusion inversion. *arXiv preprint arXiv:2412.09013*, 2024a. 7, 17

Zongsheng Yue, Jianyi Wang, and Chen Change Loy. Resshift: Efficient diffusion model for image super-resolution by residual shifting. *NeurIPS*, 36, 2024b. 6, 19

Aiping Zhang, Zongsheng Yue, Renjing Pei, Wenqi Ren, and Xiaochun Cao. Degradation-guided one-step image super-resolution with diffusion priors. *arXiv preprint arXiv:2409.17058*, 2024. 3

Kai Zhang, Jingyun Liang, Luc Van Gool, and Radu Timofte. Designing a practical degradation model for deep blind image super-resolution. In *ICCV*, pp. 4791–4800, 2021. 3

Richard Zhang, Phillip Isola, Alexei A Efros, Eli Shechtman, and Oliver Wang. The unreasonable effectiveness of deep features as a perceptual metric. In *CVPR*, pp. 586–595, 2018. 7

Weixia Zhang, Guangtao Zhai, Ying Wei, Xiaokang Yang, and Kede Ma. Blind image quality assessment via vision-language correspondence: A multitask learning perspective. In *CVPR*, pp. 14071–14081, 2023. 7

Mingyuan Zhou, Zhendong Wang, Huangjie Zheng, and Hai Huang. Long and short guidance in score identity distillation for one-step text-to-image generation. *arXiv preprint arXiv:2406.01561*, 2024a. 5

Mingyuan Zhou, Huangjie Zheng, Zhendong Wang, Mingzhang Yin, and Hai Huang. Score identity distillation: Exponentially fast distillation of pretrained diffusion models for one-step generation. In *ICML*, 2024b. 3, 4, 5, 9, 14

A APPENDIX

A.1 PROOF FOR CiD

The key point for CiD is to replace $\mathbf{z}_g = f_{\theta^*}(\mathbf{z}_t, t)$ with a optimal \mathbf{z}_h as the following identity transformation:

$$\mathbb{E}_{\mathbf{z}_h \sim \tilde{p}(\mathbf{z}_h), \mathbf{z}_l \sim p(\mathbf{z}_l)}[\langle f_\phi(\mathbf{z}_t, t), \mathbf{z}_g \rangle] = \mathbb{E}_{\mathbf{z}_h \sim \tilde{p}(\mathbf{z}_h), \mathbf{z}_l \sim p(\mathbf{z}_l)}[\langle f_\phi(\mathbf{z}_t, t), \mathbf{z}_h \rangle]. \quad (12)$$

MSE loss between SR and HR latent Eq. (6) can be formulated as:

$$\theta^* = \operatorname{argmin}_{\theta} \mathbb{E}_{\mathbf{z}_h \sim \tilde{p}(\mathbf{z}_h), \mathbf{z}_l \sim p(\mathbf{z}_l)}[\|f_\theta(\mathbf{z}_t, t) - \mathbf{z}_h\|^2]. \quad (13)$$

Apparently, the optimal solution for Eq. (13) is:

$$f_{\theta^*}(\mathbf{z}_t, t) = \mathbb{E}_{\mathbf{z}_h \sim p(\mathbf{z}_h | \mathbf{z}_t)}[\mathbf{z}_h]. \quad (14)$$

Then, CiD is proved by replacing the optimal value for \mathbf{z}_g :

$$\begin{aligned} & \mathbb{E}_{\mathbf{z}_h \sim \tilde{p}(\mathbf{z}_h), \mathbf{z}_l \sim p(\mathbf{z}_l)}[\langle f_\phi(\mathbf{z}_t, t), \mathbf{z}_g \rangle] \\ &= \mathbb{E}_{\mathbf{z}_t \sim p(\mathbf{z}_t)}[\langle f_\phi(\mathbf{z}_t, t), f_{\theta^*}(\mathbf{z}_t, t) \rangle] \\ &= \mathbb{E}_{\mathbf{z}_t \sim p(\mathbf{z}_t)}[\langle f_\phi(\mathbf{z}_t, t), \mathbb{E}_{\mathbf{z}_h \sim p(\mathbf{z}_h | \mathbf{z}_t)}[\mathbf{z}_h] \rangle] \\ &= \mathbb{E}_{\mathbf{z}_t \sim p(\mathbf{z}_t), \mathbf{z}_h \sim p(\mathbf{z}_h | \mathbf{z}_t)}[\langle f_\phi(\mathbf{z}_t, t), \mathbf{z}_h \rangle] \\ &= \mathbb{E}_{\mathbf{z}_h \sim \tilde{p}(\mathbf{z}_h), \mathbf{z}_l \sim p(\mathbf{z}_l)}[\langle f_\phi(\mathbf{z}_t, t), \mathbf{z}_h \rangle]. \end{aligned} \quad (15)$$

A.2 ALGORITHM DETAILS

In Algorithms 1 and 2, we summarize the training schemes for SD2.1-VAE16 and GenDR, respectively. Specifically, we employ a two-stage training strategy (Yin et al., 2024; Zhou et al., 2024b) for GenDR to accelerate training. In the first stage, we train GenDR as a vanilla SR model with L1 loss and perceptual loss to align the output latent distribution with the target. This processing can effectively reduce the overall training time and improve the robustness of the training. In the second stage, we train GenDR with the proposed CiDA framework to make the results more realistic.

A.3 EXPERIMENTAL DETAILS

A.3.1 DATASET PREPARATION

The diffusion-based SR aims to train a generative model creating clear details, while the images from the existing open-sourced datasets are far from uniform in terms of quality, blur, blackness, aesthetics, and compression artifacts. Thus, we conduct a dataset preselection to filter images with IQA and aesthetics metrics, where 19.2% of images from the original datasets are preserved.

A.3.2 USER AND MLLM PREFERENCE STUDIES

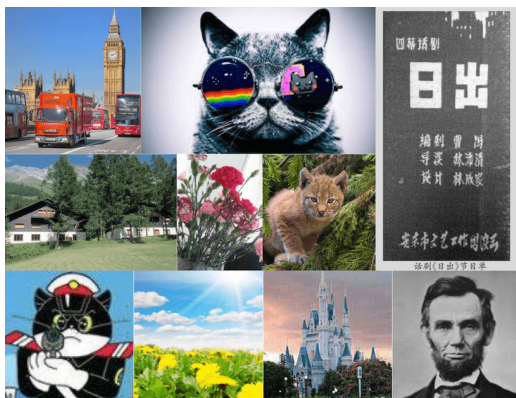


Figure 8: The LQ images used for the user study. results of various models.

User study. Following Wu et al. (2024b); Sauer et al. (2024a), we conducted a user study to evaluate the human feedback of GenDR. We randomly sampled 10 real-world LQ images from RealSet80. During testing, LQ images and two SR images restored by GenDR and SinSR/InvSR/DreamClear were presented to volunteers to select the best-matched image in quality and fidelity attributes, respectively. In Fig. 8, we show the LQ images used for the user study.

MLLM preference. Since the user study compares only 10 images and 4 methods, we additionally develop an arena using DepictQA to make pairwise comparisons between the SR re-

Algorithm 1: Training Scheme of SD2.1-VAE16

Input: Pretrained SD2.1 network ϵ_μ , SD2.1-VAE16 ϵ_θ , encoder of 16 channel VAE \mathcal{E}_{VAE} , pretrained DINOv2 encoder $\mathcal{E}_{\text{DINO}}$, $t_{\min} = 0$, $t_{\max} = 999$, $\lambda = 0.1$

Initialization $\theta \leftarrow \mu$

repeat

- Sample image \mathbf{x} and prompt c from batch \mathcal{B} ; Calculate latent with $\mathbf{z} = \mathcal{E}_{\text{VAE}}(\mathbf{x})$ and extract representation $\mathbf{h}_\mathcal{E} = \mathcal{E}_{\text{VAE}}(\mathbf{x}_h)$,
- Sample $t \in \{t_{\min}, \dots, t_{\max}\}$ and $\epsilon_t \sim \mathcal{N}(0, \mathbf{I})$, calculate forward diffusion $\mathbf{z}_t = \bar{\alpha}_t \mathbf{z}_0 + \bar{\beta}_t \epsilon_t$, and let $(\epsilon_\theta, \mathbf{h}_t) = \epsilon_\theta(\mathbf{z}_t; t, c)$;
- Update θ with $\theta = \theta - \eta \nabla_\theta \mathcal{L}_\theta$, where

$$\mathcal{L}_\theta = \|\epsilon_\theta - \epsilon_t\|_2^2 - \lambda \frac{\mathbf{h}_\mathcal{E} \cdot h(\mathbf{h}_t)}{\|\mathbf{h}_\mathcal{E}\| \|h(\mathbf{h}_t)\|}$$

until achieving convergence or the training budget is exhausted

Output: \mathcal{G}_θ

Algorithm 2: Training Scheme of GenDR

Input: Pretrained diffusion network f_μ , generator \mathcal{G}_θ , real score network f_ϕ , fake score network f_ψ , discriminative head h_h , encoder \mathcal{E} , $t_{\min} = 499$, $t_{\max} = 20$, $t_{\max} = 979$, guidance scales $\kappa = 7.5$, $\lambda_{1,2,3} = 10, 0.01, 0.1$, $\xi = 1.2$

Initialization $\theta \leftarrow \mu$, initialize LoRA ψ, ϕ , dishead h

▷ *Updating GenDR with vanilla SR loss*

repeat

- Sample latent pairs $(\mathbf{z}_h, \mathbf{z}_l)$ and prompt c from batch \mathcal{B} ; Sample $t \in \{t_{\min}, \dots, t_{\max}\}$ and $\epsilon_t \sim \mathcal{N}(0, \mathbf{I})$, and let $(\mathbf{z}_g, \mathbf{h}_t) = \mathcal{G}_\theta(\mathbf{z}_l; t, c)$
- Update \mathcal{G}_θ with $\theta = \theta - \eta \nabla_\theta \mathcal{L}_\theta$, where

$$\mathcal{L}_\theta^{(\text{reg})} = \|\mathbf{z}_g - \mathbf{z}_h\|_2^2 + \mathcal{L}_\theta^{(\text{percep})}(\mathbf{z}_g, \mathbf{z}_h)$$

until achieving convergence or processing 20M images

▷ *Updating GenDR with CiDA*

repeat

- Sample latent pairs $(\mathbf{z}_h, \mathbf{z}_l)$ and prompt c from batch \mathcal{B} ; Sample $t \in \{t_{\min}, \dots, t_{\max}\}$ and $\epsilon_t \sim \mathcal{N}(0, \mathbf{I})$, and let $(\mathbf{z}_g, \mathbf{h}_t) = \mathcal{G}_\theta(\mathbf{z}_l; t, c)$; Stop gradient for \mathbf{z}_g, ϕ ; and let $\mathbf{z}_{g,t} = \bar{\alpha}_t \text{sg}[\mathbf{z}_g] + \bar{\beta}_t \epsilon_t$, $\mathbf{z}_{h,t} = \bar{\alpha}_t \mathbf{z}_h + \bar{\beta}_t \epsilon_t$
- Update h with $h = h - \eta \nabla_h \mathcal{L}_h$, where

$$\mathcal{L}_h = \frac{1}{H'W'} \sum_{i=1}^{H'} \sum_{j=1}^{W'} \{ \ln(1 - h_h(\hat{f}_{\text{sg}[\phi]}(\text{sg}[\mathbf{z}_g]))[i, j]) + \ln h_h(\hat{f}_{\text{sg}[\phi]}(\mathbf{z}_h))[i, j] \}$$

Update ϕ with $\phi = \phi - \eta \nabla_\phi \mathcal{L}_\phi$ and ψ with $\psi = \psi - \eta \nabla_\psi \mathcal{L}_\psi$, where

$$\mathcal{L}_\phi = \|f_\phi(\mathbf{z}_{h,t}; t, c) - \mathbf{z}_h\|_2^2, \quad \mathcal{L}_\psi = \|f_\psi(\mathbf{z}_{g,t}; t, c) - \text{sg}[\mathbf{z}_g]\|_2^2$$

Sample $t \in \{t_{\min}, \dots, t_{\max}\}$ and $\epsilon_t \sim \mathcal{N}(0, \mathbf{I})$; Stop gradient for ϕ, ψ, h , get

$\omega(t) = C / \text{sg}[\|\mathbf{z}_h - f_{\phi, \kappa}(\mathbf{z}_l; t, c)\|]$, extract representation $\mathbf{h}_\mathcal{E} = \mathcal{E}(\mathbf{x}_h)$, and let $\mathbf{z}_t = \bar{\alpha}_t \mathbf{z}_g + \bar{\beta}_t \epsilon_t$

Update \mathcal{G}_θ with $\theta = \theta - \eta \nabla_\theta \mathcal{L}_\theta$, where

$$\begin{aligned} \mathcal{L}_\theta^{(\text{cida})} = & \lambda_1 \omega(t) (f_{\text{sg}[\phi], \kappa}(\mathbf{z}_t; t, c) - f_{\text{sg}[\psi], \kappa}(\mathbf{z}_t; t, c))^T ((1 - \xi) f_{\text{sg}[\phi], \kappa}(\mathbf{z}_t; t, c) - \mathbf{z}_h + \xi f_{\text{sg}[\psi], \kappa}(\mathbf{z}_t; t, c)) \\ & + \lambda_2 \frac{1}{H'W'} \sum_{i=1}^{H'} \sum_{j=1}^{W'} \ln h_h(f_{\text{sg}[\phi]}(\mathbf{z}_g))[i, j] - \lambda_3 \frac{\mathbf{h}_\mathcal{E} \cdot h(\mathbf{h}_t)}{\|\mathbf{h}_\mathcal{E}\| \|h(\mathbf{h}_t)\|} \end{aligned}$$

until processing 20M image pairs or the training budget is exhausted

Output: \mathcal{G}_θ

A.4 ADDITIONAL RESULTS FOR GENDR

A.4.1 ABLATION STUDIES

Comparison between varied prompt extraction strategies. We compared several prompt extraction strategies (Null, Fixed, DAPE (Wu et al., 2024c), Qwen2.5-7B (Team, 2024)) in Tab. 3 and found their objective metrics are quite similar. However, in visual comparison, prompts with more semantical descriptions bring more details. Fig. 9 illustrates two examples in which enriching prompts bring improved realism.

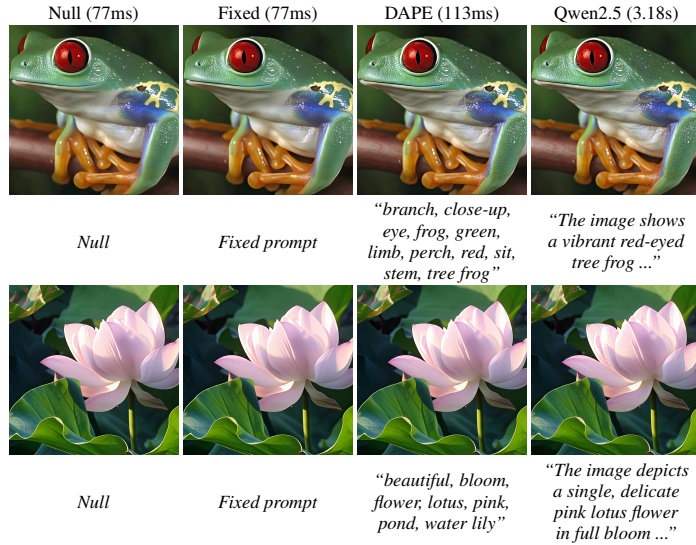


Figure 9: Comparison between images restored by GenDR with different prompt extraction methods.

To evaluate the effectiveness of our strategy for input demanding high semantic control, we test various prompt extraction strategies in the more complex face restoration task. In Fig. 10, we visualize the comparison between fixed prompts with Qwen2.5-VL generated prompt with extremely-degraded face input. Generally, GenDR with a fixed prompt can achieve comparable or even better reconstruction quality than Qwen2.5VL’s prompt, demonstrating the effectiveness and generality of the proposed strategy.

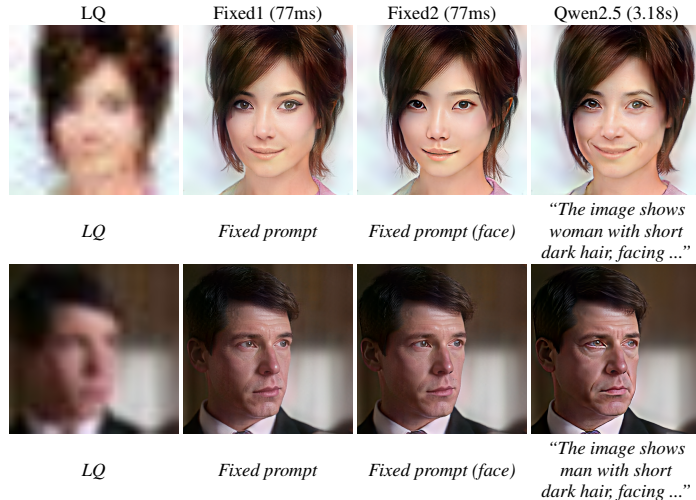


Figure 10: Comparison between images restored by GenDR with different prompt extraction methods in face restoration task. Fixed prompt (face) denotes prompts with face-related descriptions.

Comparison between varied VAEs. In Tab. 5 and Fig. 12, we examine the existing VAEs with 4/16 channels. Generally, the 16-channel-based VAEs obtain better reconstruction capability in terms of both QA metrics and subject evaluation. Our VAE is the most lightweight VAE16 that advances existing VAE4 by a large margin and VAE16 from SD3. In Fig. 11, we further visualize their latent distributions via t-SNE. The VAE4 is more uniform than VAEs and reveals clustering. This phenomenon confirms the inferior representation capability of VAE4 than VAE16 since they encode the same 50k images from ImageNet validation. Overall, these results demonstrate our findings that for T2I tasks, VAE16 brings more difficulty in generation but better reconstruction, while VAE4 is more suitable for small models but suffers from detail failure.

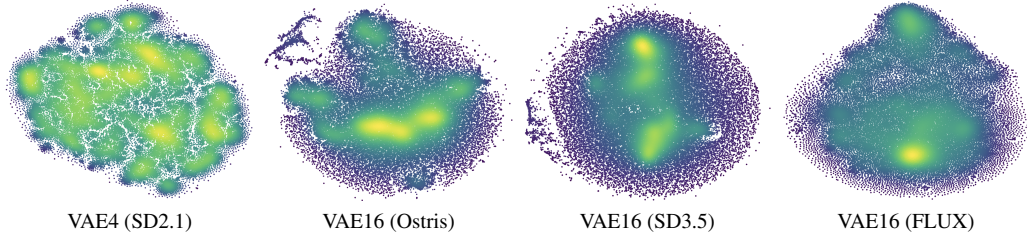


Figure 11: Visualization of the latent distribution of varied VAEs.

Comparison of varied fixed prompt. We compare several fixed prompts collected from existing work (Yue et al., 2024a; Wu et al., 2024c; Yu et al., 2024a) to find a more effective prompt for local inference embedding. The **positive prompts** are as follows:

- **P1** (InvSR (Yue et al., 2024a)): “Cinematic, high-contrast, photo-realistic, 8k, ultra HD, meticulous detailing, hyper sharpness, perfect without deformations”
- **P2** (SUPIR (Yu et al., 2024a)): “Cinematic, High Contrast, highly detailed, taken using a Canon EOS R camera, hyper detailed, photo-realistic, maximum detail, 32k, Color Grading, ultra HD, extreme meticulous detailing, skin pore detailing, hyper sharpness, perfect without deformations”
- **P3** (GenDR): “clean, high-resolution, best quality, smooth plain area, high-fidelity, clear edge, realistic detailed, 8k, perfect without deformations”
- **P4** (GenDR): “realism photo, best quality, realistic detailed, clean, high-resolution, best quality, smooth plain area, high-fidelity, clear edge, clean details without messy patterns, high-resolution, no noise, high-fidelity, clear and sharp edge, 4K, 8k, perfect without deformations, great details, 8K, photo taken in the style of Canon EOS –style raw”

The **negative prompts** are as follows:

- **N1** (InvSR (Yue et al., 2024a)): “Low quality, blurring, jpeg artifacts, deformed, over-smooth, cartoon, noisy, painting, drawing, sketch, oil painting”
- **N2** (SUPIR (Yu et al., 2024a)): “painting, oil painting, illustration, drawing, art, sketch, oil painting, cartoon, CG Style, 3D render, unreal engine, blurring, dirty, messy, worst quality, low quality, frames, watermark, signature, jpeg artifacts, deformed, low-res, over-smooth”

Table 5: Quantitative comparison between various VAEs. The best and running-up methods are highlighted in **bold** and underlined.

Figure 12: Visual comparison between various VAEs. Detail distortions arise in faces and texts for VAE4. (Zoom-in for best view.)

VAE from	SD2.1	SDXL	SD3.5	FLUX	Ours*
VAE Channel	4	4	16	16	16
#Params	0.9B	2.6B	8B	12B	0.9B
#Params (VAE)	83.65M	83.65M	83.65M	83.65M	57.27M
PSNR (dB)	27.20	27.69	30.67	32.30	30.94
SSIM	0.7857	0.8021	0.8952	0.9214	<u>0.8964</u>
LPIPS	0.1503	0.1466	0.0833	0.0702	<u>0.0752</u>

*: derived from Ostris’s vae-kl-f8-d16



Table 6: Quantitative comparison (average ClipIQA and MUSIQ) on RealLR between varied fixed (Positive/Negative) prompts with CFG=1.2.

	Null	P1	P2	P3	P4	Average
Null	0.7243/70.62	0.7234/71.61	0.7118/71.35	0.7173/71.77	0.7195/71.67	0.7193/71.40
N1	0.7240/70.58	0.7274/71.67	0.7145/71.43	0.7225/71.83	0.7243/71.73	0.7225/71.45
N2	0.7232/70.45	0.7252/71.30	0.7128/71.26	0.7200/71.70	0.7223/71.60	0.7207/71.26
N3	0.7277 /70.82	0.7274/71.77	0.7140/71.54	0.7224/ 71.93	0.7242/71.83	0.7231 / 71.58
Average	0.7248/70.62	0.7259 /71.59	0.7133/71.40	0.7206/ 71.81	0.7226/71.71	0.7214/71.42

Table 7: Quantitative comparison (average PSNR, SSIM, LPIPS, ClipIQA, MUSIQ, LIQE) on RealSR with varied CFG factors.

CFG	PSNR	SSIM	LPIPS	ClipIQA	MUSIQ	LIQE
1.0	22.78	0.7009	0.2836	0.7012	68.13	4.1690
1.1	22.67	0.6978	0.2872	0.7023	68.27	4.1909
1.2	22.55	0.6946	0.2908	0.7027	68.38	4.2076
1.3	22.43	0.6912	0.2945	0.7023	68.43	4.2172
1.4	22.31	0.6877	0.2983	0.7021	68.46	4.2225
1.5	22.31	0.6801	0.2983	0.7021	68.46	4.2227
1.6	22.31	0.6801	0.3060	0.7007	68.44	4.2147
1.7	21.92	0.6761	0.3099	0.6989	68.39	4.2004

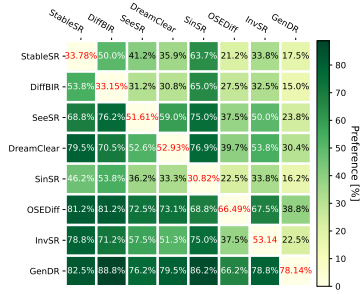


Figure 13: DepictQA preference.

Table 8: Perceptual ablation study on step distillation strategy and loss terms. We omit perceptual and MSE term of 3-7 row for simplification.

Loss	RealSR				RealSet80	
	PSNR	LPIPS	ClipIQA	MUSIQ	ClipIQA	MUSIQ
OSEDiff	24.57	0.3036	0.6829	67.30	0.7037	69.19
$\mathcal{L}^{(mse)} + \mathcal{L}^{(per)}$	26.72	0.2494	0.5235	58.19	0.5806	60.50
$\mathcal{L}^{(adv)}$	26.40	0.2731	0.6187	62.58	0.6544	65.10
$\mathcal{L}^{(vsd)}$	24.79	0.2544	0.6496	65.01	0.6911	68.82
$\mathcal{L}^{(sid)}$	24.88	0.2649	0.6511	65.39	0.7016	69.33
$\mathcal{L}^{(cid)}$	24.65	0.2527	0.6532	66.85	0.7150	70.61
$\mathcal{L}^{(cid)} + \mathcal{L}^{(adv)}$	22.62	0.2899	0.7020	68.30	0.7416	71.49
$\mathcal{L}^{(cid)} + \mathcal{L}^{(adv)} + \mathcal{L}^{(repa)}$	23.18	0.2859	0.7014	68.36	0.7424	71.57

- **N3 (GenDR):** “noise, blur, oil painting, dotted, compressed, painting, aliased edge, low quality, over-sharp, low-resolution, over-smooth, jpeg artifacts, low quality, normal quality, dirty, messy”

As shown in Tab. 6, the highest ClipIQA and MUSIQ are obtained with Null-N3 and P3-N3, respectively. We also examine the positive/negative prompts individually. In summary, P1 leads to better ClipIQA while P3 induces advanced MUSIQ. For negative prompts, the proposed N3 outperforms other settings in both attributes of ClipIQA and MUSIQ.

Comparison of varied CFG. Referring to InvSR, we implement CFG with a relatively low coefficient, *i.e.*, 1.0 to 2.0. In Tab. 7, we progressively add the CFD factor to 1.7. With increasing CFG, the FR-IQA metrics continue to drop while the NR-IQA first increases and then drops.

Extensive comparison of varied distillation strategies and loss. We include more perceptual quality comparisons for the proposed CiDA. As illustrated in Tab. 8, we compare GenDR training under various distillation loss with OSEDiff (Wu et al., 2024b) and ablate each loss term separately. Generally, the proposed CiD achieves better fidelity than VSD (Wang et al., 2024d) and SiD. Compared to OSEDiff, GenDR with CiD maintains similar NF-IQA scores but a higher LPIPS score, illustrating the effectiveness of CiD in consistency preserving. We also conduct ablation study to comprehensively figure out the effectiveness of each loss term. Generally, adding adversarial loss will introduce a perceptual performance (LPIPS) drop but also bring huge no-reference improvement.

A.4.2 TRAINING AND INFERENCE PERFORMANCE

Training cost. To comprehensively evaluate the practical cost for GenDR training with CiD/CiDA, we provide the theoretical/practical training cost (memory/time) in the same setting in Tab. 9.

- **Memory cost:** In vanilla VSD, the fake score network is fully trained, which requires updating two UNets (one-step generator and fake score network) and saving three UNets (with an additional real score network). CiD needs to update three UNets (plus extra discriminator headers for CiDA). We address this by sharing the base model and using switchable LoRA—this preserves only two UNets (one-step generator and shared score network) and optimizes fewer parameters, making CiD/CiDA feasible.
- **Time cost:** In terms of UNet forward passes, VSD/SiD executes 1 pass for generation, 2 passes for score prediction, and 1 pass for fake score updating. CiD adds an extra pass for real score network optimization, while CiDA further adds 1 more pass for GAN loss computation.
- **Practical cost:** We evaluate real training performance as follows. By using ZeRO, LoRA, and sharing strategy, CiD/CiDA requires GPU memory comparable to VSD and SiD, but slightly slows training steps by acceptable 34% and 42%.

Table 9: Training cost comparison of varied distillation strategies. “ \dagger ” represents using LoRA.

Method	Baseline	VSD	SiD	CiD	CiD \dagger	CiDA \dagger
Forward times	1	4	4	4	5	6
Additional trainable parameters (M)	0	865	865	1730	128	135
#Time per iteration (s, bs=8)	1.14	3.13	3.27	4.42	4.38	4.65
#Memory (GB, bs=8)	40.12	52.81	53.38	65.57	50.51	53.44

Inference cost. We transferred the PyTorch weight of GenDR to TensorRT fp16/int8/fp8 and deployed it on A10 and L20 for practical real-world deployment of server-side enhancement. In the following Tab. 10, we exhibit the actual performance of the overall pipeline at 1024×1024 and 1440×1440 . Specifically, for 1080p input images (1920×1080 has similar pixels as 1440×1440), GenDR can accomplish real-time restoration with throughputs of 2×1.5 images/s on A10 and 3×2.6 images/s on L20 (3×2.6 means one L20-48G can deploy 3 GenDR tasks).

Table 10: Inference cost comparison of GenDR deploying on varied GPUs.

Device-dtype	A100-fp16	A10-fp16	A10-int8	L20-fp16	L20-int8	L20-fp8
Runtime@ 1024×1024 , $\approx 720p$ (ms)	262	305	269	179	157	160
Runtime@ 1440×1440 , $\approx 1080p$ (ms)	601	721	627	424	369	381
Memory@ 1920×1440 (GB)	13.27	12.53	12.53	12.60	12.60	12.60

A.4.3 MLLM ARENA

In Fig. 13, we utilize DepictQA to make pairwise comparisons and calculate the average selected rate (in red). The GenDR receives about 78% votes, indicating its better quality than other methods.

A.4.4 VISUAL RESULTS

In Fig. 16, we provide more visual comparisons on RealSet80 (Yue et al., 2024b) between the proposed GenDR and other diffusion models. Generally, the GenDR can reasonably preserve the original information and generate more faithful details. In Fig. 17, we compare our method with OSEDiff and RealESRGAN on the KwaiSR dataset for UGC (user-generated content) SR Li et al. (2025). The proposed GenDR provides faithful reconstruction and the highest fine-grained detail restoration.

A.5 PRIMARY RESULTS FOR GENDR DISTILLED FROM SD3.5

To demonstrate the generality and expansion of GenDR, we train an SDXL-based GenDR and employ SD3.5-large as a distillation teacher. Specifically, we change the 4-channel latent space and

diffusion scheduler of a pruned SDXL (1.3B) to a 16-channel VAE space of SD3.5 and flow matching scheduler, and then use SD3.5 as fake/real prediction network of CiD to conduct SR distillation for SDXL-VAE16. The process and results of this stage are summarized in Fig. 14: SDXL-VAE16 adopts SD3’s 16-channel VAE, reduces parameters by half compared to the original SDXL, while achieving restoration quality comparable to the baseline.



Figure 14: Samples produced by SDXL (Rombach et al., 2022) (**Above**, 2.6B Diffusion Model with 4-channel VAE) and SDXL-VAE16 (**Bottom**, VAE16, 1.3B Flow Model with 16-channel VAE).

Through using SDXL-VAE16 as generator \mathcal{G}_θ and SD3.5-large as initial f_ψ and f_ϕ , we use a flow-matching adapted Eq. (9) to train primary SDXL-based GenDR, termed GenDR-1.3B. We provide the primary results of the 10k iteration training in Fig. 15.

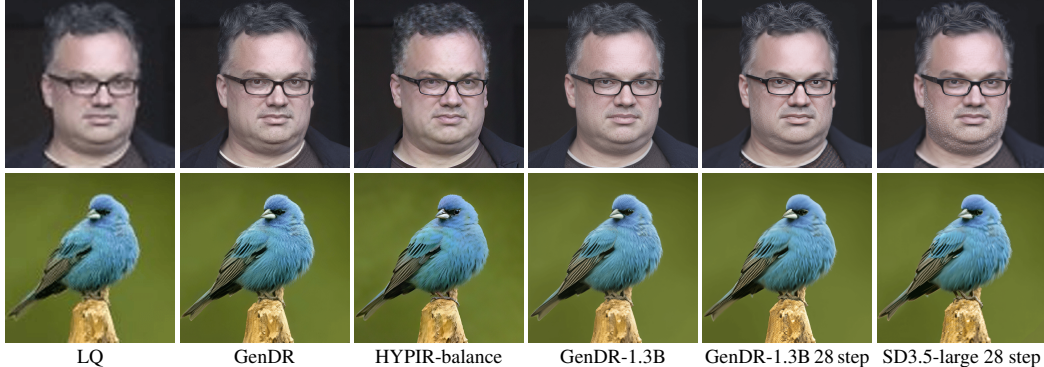


Figure 15: Samples produced by GenDR, HYPiR (Lin et al., 2025), SDXL-based GenDR, and SD3.5-large with ControlNeXt (Peng et al., 2024).

A.6 ADDITIONAL RESULTS FOR SD2.1-VAE16

A.6.1 QUANTITATIVE REUSLTS

To further verify the usability of SD2.1-VAE16, we provide detailed results of GenEval (Ghosh et al., 2023) and additional CLIP results in Tab. 4. Generally, the proposed SD2.1-VAE16 is slightly lagged behind SD2.1 (similar CLIP but lower GenEval), which is aligned with our expectation since increasing the latent space dimension will introduce a generation difficulty (Esser et al., 2024).

Table 11: Comparison of T2I methods.

Model	#Params	GenEval↑	CLIP↑
PixArt- α	0.6B	0.48	0.316
SD1.5	0.9B	0.43	0.322
SD2.1	0.9B	<u>0.50</u>	0.30
SD-Turbo	0.9B	-	<u>0.335</u>
SDXL	2.6B	0.55	0.343
SD2.1-VAE16	0.9B	0.48	0.323

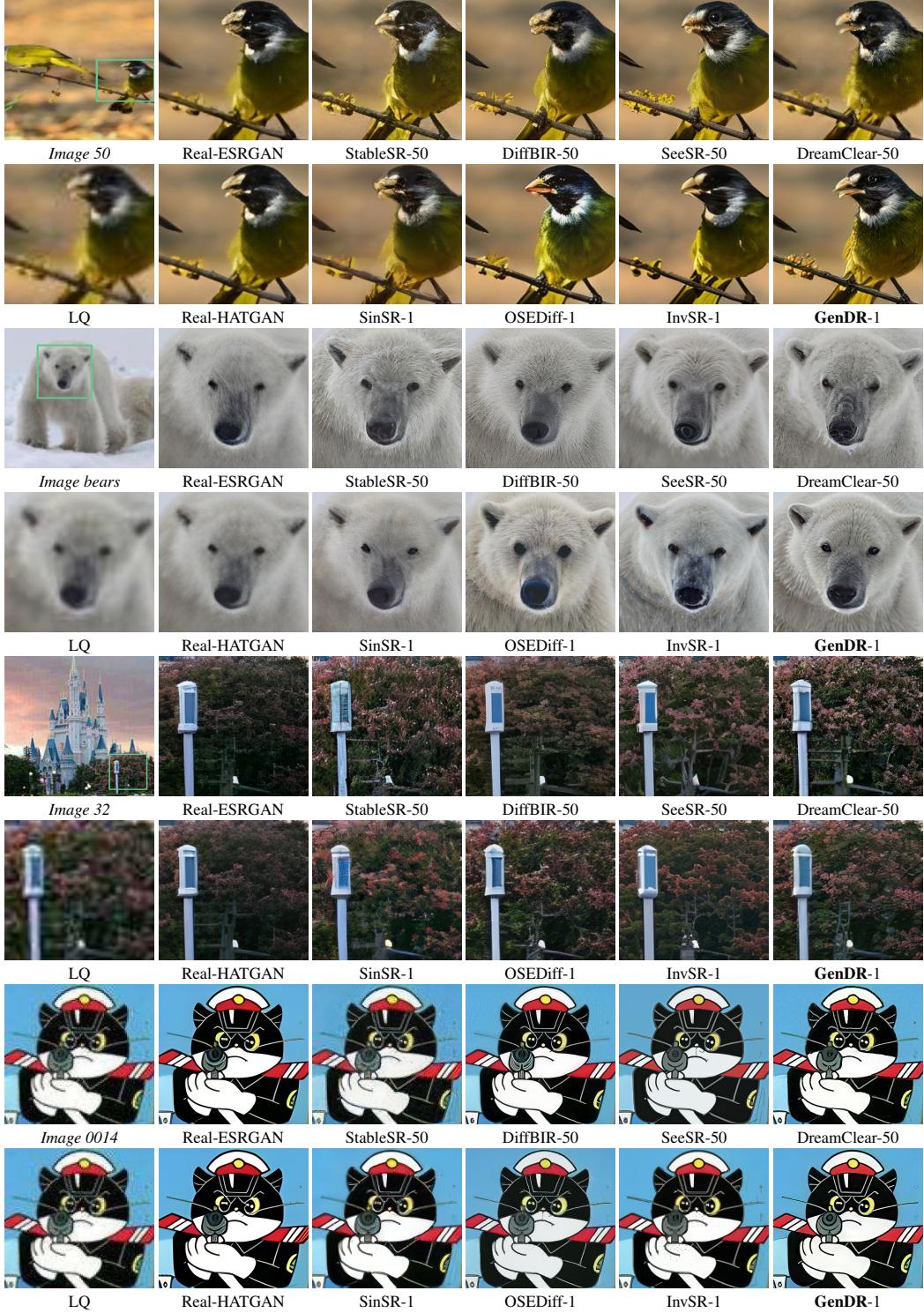
A.6.2 QUALITATIVE RESULTS

In Fig. 18, we show the images generated by the proposed SD2.1-VAE16 with the following prompts:

- An astronaut riding a horse in the forest.
- A girl examining an ammonite fossil.
- A chimpanzee sitting on a wooden bench.
- A penguin standing on a sidewalk.
- A goat wearing headphones.
- Dreamy puppy surrounded by floating bubbles.
- An elephant walking on the Great Wall.
- An oil painting of two rabbits in the style of American Gothic, wearing the same clothes as in the original.
- A woman wearing a red scarf.
- Motion.
- A squirrel driving a toy car.
- A giant gorilla at the top of the Empire State Building.
- A bowl with rice, broccoli and a purple relish.
- Stars, water, brilliantly, gorgeous large scale scene, a little girl, in the style of dreamy realism.
- A cat reading a newspaper.
- A woman wearing a cowboy hat face to face with a horse
- A watermelon chair.
- A photo of llama wearing sunglasses standing on the deck of a spaceship with the Earth in the background.
- Pirate ship trapped in a cosmic maelstrom nebula, rendered in cosmic beach whirlpool engine, volumetric lighting, spectacular, ambient lights, light pollution, cinematic atmosphere, art nouveau style, illustration art artwork by SenseiJaye, intricate detail.

B THE USE OF LARGE LANGUAGE MODELS (LLMs)

We use Large Language Models in this research project to assist with various aspects of the writing and research process, including text polishing and refinement, and grammar enhancement.

Figure 16: Visual comparison of GenDR with other methods for $\times 4$ task. (Zoom-in for best view.)

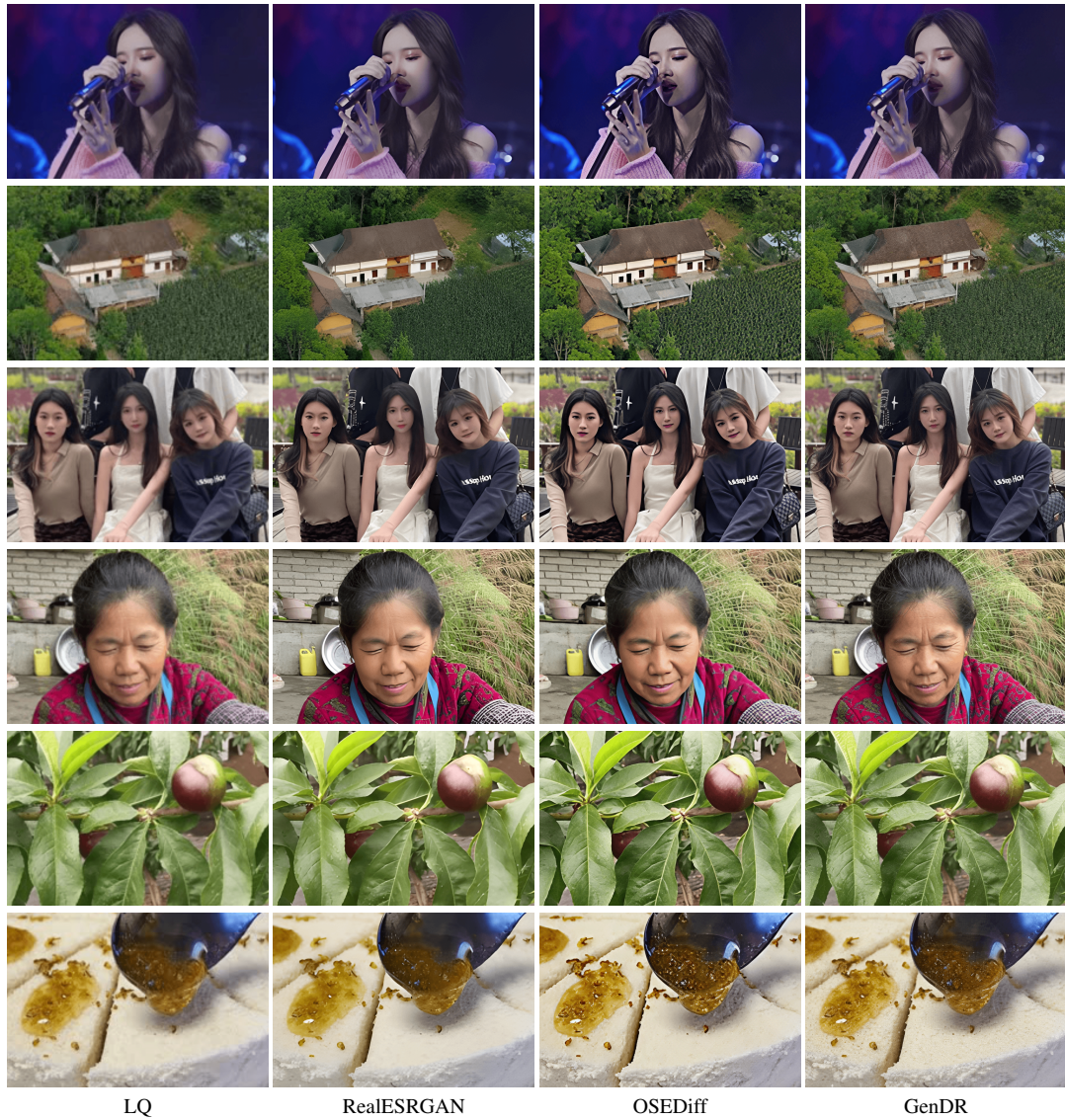


Figure 17: Visual comparison of GenDR with other methods for UGCSR. (Zoom in for best view.)



Figure 18: 1024^2 px and 512^2 px samples produced by SD2.1-VAE16.